PHYSICS OF FLUIDS **25**, 052102 (2013)

A mapping method for distributive mixing with diffusion: Interplay between chaos and diffusion in time-periodic sine flow

Conor P. Schlick,[1,a)] Ivan C. Christov,[1,2,b)] Paul B. Umbanhowar,[3] Julio M. Ottino,[2,3,4] and Richard M. Lueptow[3,4,c)]
[1]*Department of Engineering Sciences and Applied Mathematics, Northwestern University, Evanston, Illinois 60208, USA*
[2]*Department of Chemical and Biological Engineering, Northwestern University, Evanston, Illinois 60208, USA*
[3]*Department of Mechanical Engineering, Northwestern University, Evanston, Illinois 60208, USA*
[4]*The Northwestern Institute on Complex Systems (NICO), Northwestern University, Evanston, Illinois 60208, USA*

(Received 1 October 2012; accepted 13 February 2013; published online 14 May 2013)

We present an accurate and efficient computational method for solving the advection-diffusion equation in time-periodic chaotic flows. The method uses operator splitting, which allows the advection and diffusion steps to be treated independently. Taking advantage of flow periodicity, the advection step is solved using a mapping method, and diffusion is "added" discretely after each iteration of the advection map. This approach results in the construction of a composite mapping matrix over an entire period of the chaotic advection-diffusion process and provides a natural framework for the analysis of mixing. To test the approach, we consider two-dimensional time-periodic sine flow. By comparing the numerical solutions obtained by our method to reference solutions, we find qualitative agreement for large time steps (structure of concentration profile) and quantitative agreement for small time steps (low error). Further, we study the interplay between mixing through chaotic advection and mixing through diffusion leading to an analytical model for the evolution of the intensity of segregation with time. Additionally, we demonstrate that our operator splitting mapping approach can be readily extended to three dimensions. © *2013 AIP Publishing LLC*. [http://dx.doi.org/10.1063/1.4803897]

I. INTRODUCTION

At the heart of most mixing phenomena is the advection-diffusion equation, which describes the physical process of a passive scalar quantity (species) diffusing while simultaneously being carried along (and stirred) by a flow.[1] In the absence of diffusion, there are many ways to solve the advection equation, which is both hyperbolic and time-reversible. Thus, even in complicated domains and in the presence of chaotic velocity fields, determining how a scalar is advected can be accomplished quite efficiently. One way of doing so is a class of techniques known as *mapping methods*. By decomposing the domain into a grid, and computing the proportion of each grid cell that is transported to any other, the dynamical problem of advection can be reduced to multiplication by a mapping matrix.

[a)]Electronic mail: conorschlick2015@u.northwestern.edu
[b)]Present address: Department of Mechanical and Aerospace Engineering, Princeton University, Princeton, New Jersey 08544, USA.
[c)]Electronic mail: r-lueptow@northwestern.edu

Spencer and Wiley[2] proposed such an approach in 1951 for studying the coarse-grained mixing properties of a flow. The idea is also popular in dynamical systems: Hsu[3] developed a cell-to-cell mapping that approximates the behavior of a nonlinear dynamical system, Wang *et al.*[4] proposed a cell-map method for approximating the Poincaré section of time-periodic chaotic dynamics, and Froyland *et al.*[5,6] used mapping matrices ("transfer operators" in their language) to detect coherent and invariant structures in geophysical flows[7] (see also Ref. 8 for an overview). Anderson and co-workers[9–11] have successfully used the mapping method of Spencer and Wiley[2] to study realistic mixing flows by advecting the boundaries of grid cells and then projecting the deformed grid onto the original one to obtain the mapping matrix that solves the purely advective problem.

Thus, while different types of mapping methods and their applications have been studied,[3–11] the main research effort has focused on purely distributive mixing by advection. However, even a small amount of diffusion leads to a governing equation that is parabolic and, thus, irreversible, which has significant implications for chaotic flows.[12] Irreversibility and the presence of both first and second-order spatial derivatives make it more difficult to solve the governing equation numerically. How to effectively exploit the simplicity of mapping methods for the full advection-diffusion problem remains an open question that we address in the present work.

One drawback to mapping methods is that, like any numerical discretization, they introduce *artificial (numerical) diffusivity*[13,14] even for purely advective problems.[15] Recently, it has been proposed that the inherent numerical diffusion in the mapping method can be considered analogous to molecular diffusion, and thus the mapping method can be used to solve some advection-diffusion problems.[16] While seemingly attractive, there are, however, several challenges associated with this approach. To start with, numerical diffusion is controlled by the spatial resolution rather than imposed independently of it by the physics of the problem. Yet, choosing the correct spatial resolution corresponding to a given diffusivity requires prior knowledge of the flow. Furthermore, numerical diffusion does not necessarily have the same physical behavior as molecular diffusion (i.e., it may not take the form of a Laplacian).[17]

The importance of incorporating diffusion in a physically realistic manner becomes apparent when considering time-dependent flows. Molecular diffusion, when coupled with mixing, is highly anisotropic in such problems; most mixing takes place normal to the direction of strong stretching. Time-dependent flows can give rise to chaotic advection, which leads to the creation of thinning striations through stretching and folding, while diffusion mixes efficiently across these concentration gradients.[18] Such details become important when studying mixing of chemically reactive species because the reaction rate is highly dependent on both the diffusivity of the reactants and, if the diffusivity is small, the interface between the two reactants.[19] The interplay between small-scale mixing and reactions is important for very fast non-premixed reactions such as in combustion and flames.[20,21] Hence, both the diffusive and advective time scales need to be properly resolved to obtain accurate simulations.

To this end, we study the effectiveness of several mapping-based numerical techniques for advection-diffusion in time-periodic sine flow,[22,23] a two-dimensional flow consisting of the periodic application of orthogonal sinusoidal velocity profiles in a plane. Time-periodic sine flow is a convenient model system in which to test approaches to solving the advection-diffusion equation because the velocity field and tracer trajectories (on which the mapping method is based) can be found analytically. Moreover, time-periodic sine flow provides a well-characterized chaotic velocity field under which we study mixing of a scalar. Specifically, through a simple analytical model, we relate the evolution of the quality of mixing to the striation thickness distribution produced by the flow and to the size of unmixed islands in the flow field.

This paper is organized as follows. In Sec. II, we present and benchmark our method for solving the advection-diffusion equation using operator splitting in conjunction with a mapping method. In Sec. III, we employ our numerical method to study the interplay between chaotic advection and diffusion in time-periodic sine flow. Finally, in Sec. IV, we demonstrate how the numerical method can be applied to a three-dimensional advection-diffusion problem.

TABLE I. Names and abbreviations of the numerical methods for solving the advection-diffusion equation (1) considered in this work, presented in order of complexity.

Method	Abbr.	Description
Particle tracking method	PT	Tracer trajectories are computed in the absence of diffusion.
Numerical diffusion (mapping) method[16]	ND	Numerical diffusion is assumed to mimic physical diffusion; can be used to calculate quality of mixing, but cannot resolve fine structures in the concentration field.
Modified mapping method with $\Delta t = T$[28]	MM	Mapping method with operator splitting, time step equal to one period; easy to implement, but splitting error cannot be controlled because the time step is fixed by T.
Modified mapping method with $\Delta t < T$ (Section II A)	MM	Mapping method with operator splitting, time step less than one period; easy to implement and more accurate than MM method with $\Delta t = T$, but can exhibit increased numerical diffusion on coarse grids.
Galerkin spectral method[29,30]	GS	GS solution is very close to the exact one if enough modes are taken; difficult to implement in complex geometries.

II. MAPPING METHOD WITH DIFFUSION

Our goal is to solve the advection-diffusion equation for the unsteady concentration profile $c(\boldsymbol{x}, t)$ of a species in a domain Ω. In dimensionless variables, the governing equation is[24]

$$\frac{\partial c}{\partial t} + \boldsymbol{u} \cdot \nabla c = \frac{1}{\mathrm{Pe}} \nabla^2 c, \qquad \boldsymbol{x} \in \Omega, \quad t > 0, \tag{1}$$

where $\boldsymbol{u}(\boldsymbol{x}, t)$ is the given divergence-free ($\nabla \cdot \boldsymbol{u} = 0$) advective velocity vector field, t is time, and $\mathrm{Pe} = UL/D$ is the Péclet number, where U is a characteristic velocity, L is a characteristic length scale, and D is the diffusivity of the tracer. Typically, Neumann (no flux) or periodic boundary conditions are imposed, which ensures that the total species mass within the domain, $\int_\Omega c(\boldsymbol{x}, t) d\boldsymbol{x}$, remains constant in time.[25] In applications, a wide range of Péclet numbers are encountered: for example, $\mathrm{Pe} \sim 10^2$ for laminar flames,[26] $\mathrm{Pe} \sim 10^3$ to 10^5 for molecular dyes in typical microfluidic water/glycerol solutions,[27] $\mathrm{Pe} \sim 10^5$ for granular materials in rotating tumblers,[28] and $\mathrm{Pe} \sim 10^{10}$ for turbulent reactive flows.[26]

To solve Eq. (1), we propose a mapping method based on the original concept of Spencer and Wiley,[2] but modified to include diffusion using the operator splitting approach introduced by Christov *et al.*[28] We extend the latter method to allow for small splitting time steps, which improves the method's accuracy. We compare the results using both small and large splitting time steps against the solution found by a spectral method, which we use as the reference ("exact") solution. A summary of the various methods used in the paper is given in Table I.

A. Modified mapping (MM) method

Because tracking material lines (cell boundaries), as is done in a number of mapping methods,[9–11] advected by complex flows is a difficult numerical problem,[31] Singh *et al.*[32] developed a simplified mapping method in which the mapping matrix is constructed by advecting a group of tracer particles placed in each grid cell, instead of tracking the deformation of the cell. This simplified approach has been used to optimize micromixers,[33] and to find eigenmodes of mixing in fluid[15] and granular[28] flows.

To implement the method (in two dimensions), the domain Ω is divided into an N_x by N_y grid ($N_x N_y$ total cells). For simplicity, we assume that Ω is rectangular and that N_x and N_y can be chosen such that each grid cell is a square. Next, n^2 tracer particles are uniformly distributed inside each cell (we use $n = 100$) at a given initial time t_0. Each tracer particle is then advected from $t = t_0$ to $t = t_0 + \Delta t$ by solving the set of ordinary differential equations $d\boldsymbol{x}(t)/dt = \boldsymbol{u}(\boldsymbol{x}(t), t)$, with $\boldsymbol{x}(t_0)$ as the specified initial location of the particle, and the cell in which it is located at $t = t_0 + \Delta t$ is then

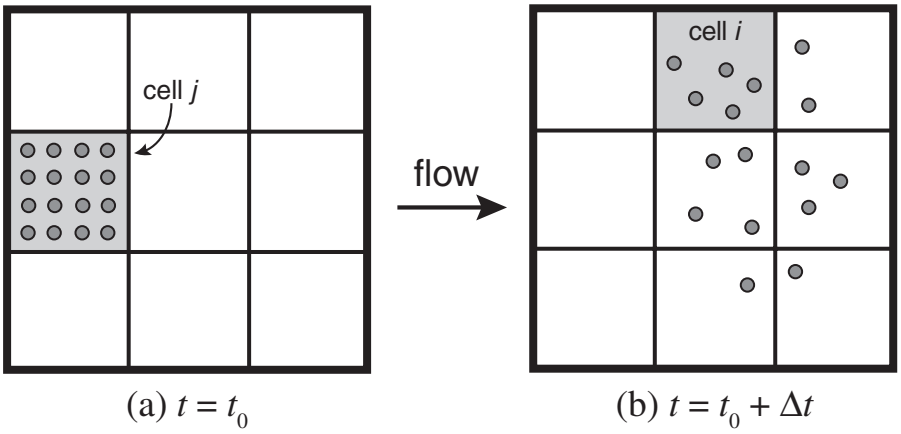

FIG. 1. Illustration of the simplified mapping method[32] and the construction of the mapping matrix. Tracer particles are distributed uniformly in cell j at (a) $t = t_0$ and advected by the flow up to (b) $t = t_0 + \Delta t$. Then, the distribution of particles is projected onto the original grid to obtain the proportion of each cell that was transported to any other. In this example, 5 of the 16 tracer particles from cell j are advected to cell i, so $\mathbf{\Phi}^{(i,j)}_{t_0 \to t_0+\Delta t} = \frac{5}{16}$.

determined (see Figure 1). This allows for the calculation of the entries in the matrix $\mathbf{\Phi}_{t_0 \to t_0+\Delta t}$:

$$\mathbf{\Phi}^{(i,j)}_{t_0 \to t_0+\Delta t} = \frac{\text{number of tracers from cell } j \text{ that end in cell } i}{\text{total number of tracers that started in any cell } (= n^2)}. \tag{2}$$

Therefore, $\mathbf{\Phi}_{t_0 \to t_0+\Delta t}$ is an $N_x N_y$ by $N_x N_y$ matrix that determines how the material in the domain is redistributed by the advective velocity field $\boldsymbol{u}$. We implement forward particle tracking (i.e., seed the tracers at $t = t_0$ and advect them forward), although backward particle tracking (i.e., seed the tracers at $t = t_0 + \Delta t$ and determine where they originate) can also be used.[4,34] While backward particle tracking leads to a better visual representation of the effect of the flow (because particles are uniformly distributed at the final, instead of the initial, time), we use enough tracer particles (i.e., $n = 100$) so that the difference (both visual and quantitative) between the two methods is negligible.[35]

We define $\boldsymbol{c}(t)$ to be a column vector in which the entry in row j represents the concentration in cell j, with the cells being enumerated from 1 to $N_x N_y$. The given initial concentration distribution provides $\boldsymbol{c}(t_0)$, hence the concentration after a time of Δt has elapsed is (approximately) given by $\boldsymbol{c}(t_0 + \Delta t) = \mathbf{\Phi}_{t_0 \to t_0+\Delta t} \boldsymbol{c}(t_0)$. If the flow is periodic with period T (i.e., $\boldsymbol{u}(\boldsymbol{x}, t) = \boldsymbol{u}(\boldsymbol{x}, t + T)$), then

$$\mathbf{\Phi}_{t_0 \to t_0+T} = \mathbf{\Phi}_{t_0+mT \to t_0+(m+1)T} \equiv \mathbf{\Phi}_{t_0,T} \tag{3}$$

for any integer m, and the subscript "t_0, T" is shorthand notation for "$t_0 \to t_0 + T$." Thus, the concentration profile after m periods takes the form

$$\boldsymbol{c}(mT) = \left(\mathbf{\Phi}_{0,T}\right)^m \boldsymbol{c}(0), \tag{4}$$

where we have set $t_0 = 0$.

We incorporate diffusion into the mapping method via operator splitting[36] of the advection-diffusion problem as implemented by Christov *et al.*[28] Separating the advection-diffusion problem into individual advection and diffusion steps, each of which is simpler to solve than the original problem, has been used in the literature in an *ad hoc* manner in a number of contexts ranging from diffusion of magnetic field lines in fast dynamos[37,38] to tracer microstructure in turbulent flows.[39] In the present work, we show that these phenomenological approaches can be formalized using the mathematical idea of operator splitting, which is an efficient approach to simulating scalar mixing,[40] and we quantify the error committed in performing such splitting. More recently, Gorodetskyi *et al.*[41] proposed an alternative approach, similar to that of Jones,[42] that includes diffusion in a mapping method by adding a stochastic forcing term to the equations for the advection of tracer particles.

Following Christov *et al.*,[28] we include the effects of diffusion in the mapping method described above using Marchuk–Yanenko operator splitting[43] for the advection-diffusion equation (1) with

splitting time step $\Delta t = T$ for a T-periodic flow. To evolve the concentration from $t = mT$ to $t = (m+1)T$ using this operator-splitting scheme, we first solve the advection problem

$$\frac{\partial c^*}{\partial t} = -\boldsymbol{u} \cdot \nabla c^*, \qquad t \in [mT, (m+1)T], \tag{5}$$

for $c^*((m+1)T)$ using $c(mT)$ as the initial condition. Next, we solve the diffusion problem

$$\frac{\partial c}{\partial t} = \frac{1}{\mathrm{Pe}} \nabla^2 c, \qquad t \in [mT, (m+1)T], \tag{6}$$

for $c((m+1)T)$ using $c^*((m+1)T)$ as the initial condition. Equation (5) is solved with the mapping method yielding $\boldsymbol{c}^*((m+1)T) = \boldsymbol{\Phi}_{0,T}\boldsymbol{c}(mT)$. To solve Eq. (6), we use a backward Euler time discretization (as in the classical Marchuk–Yanenko operator splitting[43]) with time step $\Delta t = T$ and $\boldsymbol{c}^*((m+1)T)$ as the initial condition at $t = mT$, arriving at

$$\frac{\boldsymbol{c}((m+1)T) - \boldsymbol{c}^*((m+1)T)}{T} = \frac{1}{\mathrm{Pe}} \boldsymbol{\nabla}_h^2 \boldsymbol{c}((m+1)T). \tag{7}$$

The subscript h indicates that the Laplacian operator is discretized in space (using here the standard 5-point formula defined on the same grid as the mapping method), meaning that $\boldsymbol{\nabla}_h^2$ is a matrix.

Finally, as in Christov *et al.*,[28] from Eq. (7) we obtain a modified mapping matrix for a time-periodic advective-diffusive process:

$$\boldsymbol{c}((m+1)T) = \widetilde{\boldsymbol{\Phi}}_{0,T}\boldsymbol{c}(mT), \quad \text{where} \quad \widetilde{\boldsymbol{\Phi}}_{0,T} = \left[\mathbf{I} - \frac{T}{\mathrm{Pe}} \boldsymbol{\nabla}_h^2\right]^{-1} \boldsymbol{\Phi}_{0,T}. \tag{8}$$

Computing $\boldsymbol{c}$ using Eq. (8) is what we refer to as the "modified mapping method" (MM method) with $\Delta t = T$. Note that it is possible to take an arbitrarily large splitting time step because Marchuk–Yanenko operator splitting is *unconditionally stable* thanks to the implicit time discretization in Eq. (7) and the fact that the mapping matrix has spectral norm $\|\boldsymbol{\Phi}_{0,T}\| < 1$.[15] However, Marchuk–Yanenko operator splitting is formally first-order accurate in time, so the error is $\mathcal{O}(\Delta t)$, where $\Delta t = T$ in this case.[44]

The discretized Laplacian $\boldsymbol{\nabla}_h^2$ is a banded matrix and $\boldsymbol{\Phi}_{0,T}$ is sparse for most flows, so the matrix manipulations in Eq. (8) are computationally efficient. As a result, the MM method is relatively cheap and simple to implement. However, there are still some drawbacks. Most importantly, the method is derived for a time-periodic flow (with period T) and a splitting time step $\Delta t = T$. The latter makes the calculation quite simple, since the flow domain is the same after every iteration of the mapping matrix, meaning $\boldsymbol{\Phi}_{0,T}$ and $\boldsymbol{\nabla}_h^2$ can be constructed once and used for any number of periods of the process. However, this means that the effects of diffusion are incorporated only once at the end of every advection period, instead of being accounted for continuously with advection during this time. In practice, this works well, for example, for granular flow,[28] however the splitting error incurred and its accumulation over time must be quantified, as we do in Sec. II D.

Naturally, there is also "numerical diffusion" (due to both the approximation of the advection operator by $\boldsymbol{\Phi}_{t_0 \to t_0+\Delta t}$ and the diffusion operator by $\boldsymbol{\nabla}_h^2$), which becomes negligible as $N_x, N_y \to \infty$. Similarly, the $\mathcal{O}(\Delta t)$ splitting error vanishes as $\Delta t \to 0$. However, in the description of the scheme above, we set $\Delta t = T$, which is typically not small. To improve on this, here we generate a family of mapping matrices, each corresponding to a different portion of the period of the flow.[45] For example, we could construct four mapping matrices $\boldsymbol{\Phi}_{0 \to T/4}$, $\boldsymbol{\Phi}_{T/4 \to T/2}$, etc., and then apply Eq. (8) for each of the four time increments Δt (i.e., the MM method with $\Delta t = T/4$). However, this requires more matrix multiplications by an appropriate $\boldsymbol{\Phi}_{t_0 \to t_0+\Delta t}$, which could lead to increased numerical diffusion and computational time. As a result, there is a trade-off between the number of time increments ($T/\Delta t$) used and the problems of numerical diffusion and computational time. In Sec. II D we investigate this issue both qualitatively and quantitatively.

B. Galerkin spectral (GS) method

As an independent check of the MM method described above, we compare our numerical results to those obtained by a Galerkin spectral (GS) method. Following the approach of Cerbelli *et al.*[29,30]

(see also Ref. 46), we first define the set of basis functions $\{\psi_{\boldsymbol{k}}(\boldsymbol{x})\}$ as the solutions of the associated eigenvalue problem $\nabla^2\psi_{\boldsymbol{k}} + \lambda_{\boldsymbol{k}}\psi_{\boldsymbol{k}} = 0$ with the same boundary conditions as the advection-diffusion equation (1). Depending on the dimension of Ω, $\boldsymbol{k}$ could be a multi-index (e.g., in two dimensions $\boldsymbol{k} = (k_1, k_2)$). From the Sturm–Liouville theorem, the set $\{\psi_{\boldsymbol{k}}(\boldsymbol{x})\}$ forms an orthogonal basis of $L^2(\Omega)$ (the set of square integrable functions on Ω).[47] Thus, the concentration $c(\boldsymbol{x}, t)$ can be approximated by a linear combination of the basis functions $\psi_{\boldsymbol{k}}(\boldsymbol{x})$ with time-dependent coefficients $\phi_{\boldsymbol{k}}(t)$:

$$c(\boldsymbol{x}, t) = \sum_{\boldsymbol{k}} \phi_{\boldsymbol{k}}(t)\psi_{\boldsymbol{k}}(\boldsymbol{x}). \tag{9}$$

Substituting this expression into the advection-diffusion equation (1), multiplying through by the complex conjugate of $\psi_{\boldsymbol{p}}(\boldsymbol{x})$ (denoted by an overline), integrating over the domain Ω, and using the orthogonality relation for the eigenfunctions gives

$$\frac{d\phi_{\boldsymbol{p}}}{dt} = \sum_{\boldsymbol{k}} \mathbf{C}^{(\boldsymbol{p};\boldsymbol{k})}\phi_{\boldsymbol{k}} - \frac{\lambda_{\boldsymbol{p}}}{\mathrm{Pe}}\phi_{\boldsymbol{p}}, \quad \text{where} \quad \mathbf{C}^{(\boldsymbol{p};\boldsymbol{k})} = -\frac{\int_\Omega \bar{\psi}_{\boldsymbol{p}}\,[\boldsymbol{u}\cdot\nabla\psi_{\boldsymbol{k}}]\,d\boldsymbol{x}}{\int_\Omega |\psi_{\boldsymbol{p}}|^2\,d\boldsymbol{x}}. \tag{10}$$

We note that $\psi_{\boldsymbol{k}}$ can be a complex-valued function only because it is convenient to represent the eigenfunctions of ∇^2 on rectangular domains as complex exponentials. To compare with the spatially discrete mapping methods, the concentration (as given by Eq. (9)) is averaged across 25 points evenly distributed in each grid cell (similar to Figure 1(a)).

The GS method reduces solving the advection-diffusion equation (1) to a problem of solving a coupled system of ordinary differential equations. If the basis functions $\psi_{\boldsymbol{k}}$ are known explicitly, then all the coefficients can be determined, thus putting the system in the form $d\boldsymbol{\phi}(t)/dt = \mathbf{A}(t)\boldsymbol{\phi}(t)$, where $\boldsymbol{\phi}(t)$ is a column vector containing the values of $\phi_{\boldsymbol{k}}(t)$ and $\mathbf{A}(t)$ is the matrix representing the action of the right-hand side of the first equation in (10).[29,30,46] Note that $\mathbf{A}$ may depend on t because $\boldsymbol{u}$ can be a function of t.

In contrast to the MM method, the GS method does not require decoupling of the advection and diffusion subproblems. The source of error in the GS method is the truncation of the expansion at a finite number of modes and the discretization of $d\boldsymbol{\phi}(t)/dt = \mathbf{A}(t)\boldsymbol{\phi}(t)$ in time. In general, the time-discretization error can be made arbitrarily small by taking small time steps and/or using a high-order integration scheme. The main advantage of the GS method is that, under suitable conditions, the coefficients $\phi_{\boldsymbol{k}}$ in the expansion in Eq. (9) decrease in magnitude exponentially with $|\boldsymbol{k}|$ (if the boundary conditions are periodic), thus highly accurate solutions are obtained with a small number of modes.[48] In the rest of this paper, the set of modes indexed by $\boldsymbol{k}$ are such that $-N \le k_1, k_2 \le N$, giving a total of $(2N+1)^2$ modes in two dimensions.

The main disadvantages of the GS method are (i) the need to have a domain Ω for which the eigenfunctions $\psi_{\boldsymbol{k}}$ can be found analytically, and (ii) the need to evaluate the integrals in the definition of $\mathbf{C}$ in Eq. (10). Another drawback is that the GS method is not immediately applicable if only trajectories of tracers (instead of a smooth velocity field) are known. Meanwhile, mapping methods can be applied with only the knowledge of the trajectories of tracers obtained from, say, experimental observations (see Figure 1). Additionally, $\mathbf{C}^{(\boldsymbol{k};\boldsymbol{p})}$ is not necessarily sparse for a generic velocity field $\boldsymbol{u}$, which could make solving $d\boldsymbol{\phi}(t)/dt = \mathbf{A}(t)\boldsymbol{\phi}(t)$ inefficient. Conversely, in the MM method, the matrices appearing in Eq. (8) will almost always be sparse.

C. Time-periodic sine flow (TPSF)

For the advective velocity field, we choose time-periodic sine flow (TPSF), shown schematically in Figure 2. It is a particular type of "eggbeater flow," i.e., a velocity profile that alternates between unidirectional orthogonal components.[22] TPSF has been studied by Liu *et al.*[23] in quantifying chaotic mixing in aperiodic flows (by randomly modulating the period of TPSF). More recently, TPSF has been used as a canonical example of laminar chaotic mixing[49] and for evaluating mapping methods.[15,16,41] The velocity field of TPSF, which is defined on the unit square ($0 \le x, y \le 1$) with

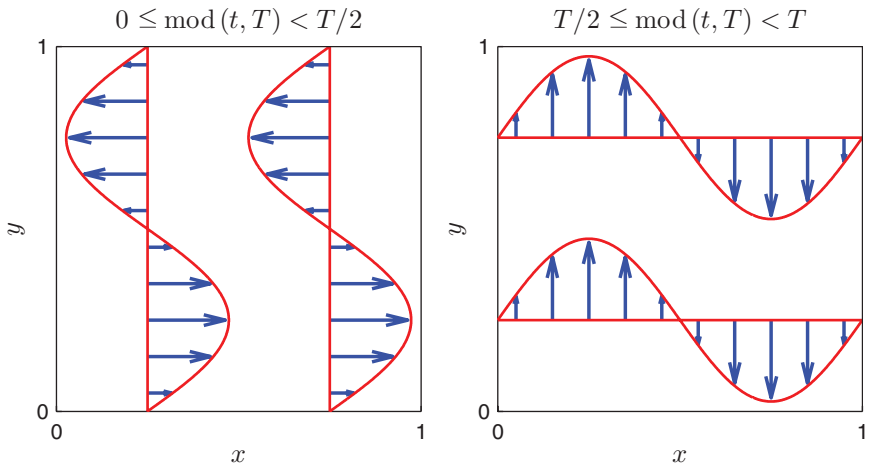

FIG. 2. Schematic of the velocity field of time-periodic sine flow (TPSF).

periodic boundary conditions, is

$$\boldsymbol{u}(x,y,t) = \begin{cases} \sin(2\pi y)\,\hat{\boldsymbol{x}}, & 0 \le \mathrm{mod}(t,T) < \frac{T}{2}, \\ \sin(2\pi x)\,\hat{\boldsymbol{y}}, & \frac{T}{2} \le \mathrm{mod}(t,T) < T, \end{cases} \tag{11}$$

where $\mathrm{mod}(t,T) = t - qT$ with q being an integer such that $0 \le t - qT < T$. The period of the flow T can be any positive number, and $T/2$ represents how long the flow acts in one direction before switching to the orthogonal one.

While TPSF is difficult to produce experimentally, it is relevant for the present study because it is simple and periodic while still being nonlinear. The mapping method for TPSF is convenient in that an exact analytic solution for the trajectories of tracers can be found in the absence of diffusion. This permits the comparison of results using the MM method with the addition of diffusion both once every period and several times per period, without the need to worry about error introduced in the integration of tracer trajectories. Since the domain is square, we can also set $N_x = N_y$ for all our calculations. Furthermore, this flow allows efficient implementation of the GS method because most of the coefficients $\mathbf{C}^{(p;k)}$ from Eq. (10) are zero, resulting in a tridiagonal matrix $\mathbf{A}$ (see Ref. 29 for details).

Depending on the period T of the flow, tracer trajectories in TPSF can exhibit either regular or chaotic behavior. We consider two cases: $T = 1.6$ and $T = 0.8$. Shorter periods result in too little stretching to obtain significant mixing, while longer periods do not increase mixing substantially. Final concentration states of TPSF with $\mathrm{Pe} = \infty$ (no diffusion) after 1 and 5 periods are shown in Figure 3. In this, and all of our subsequent simulations, half of the domain ($x > 1/2$) initially has a concentration of 1 (white), while the other half has a concentration of 0 (black), as shown in Figure 3(a). For $T = 1.6$ the flow is fully chaotic throughout the entire domain, while for $T = 0.8$ the flow is partially chaotic having both chaotic and regular regions (four Kolmogorov–Arnold–Moser (KAM) islands). In Figures 3(c) and 3(e), there are some gray areas (concentration not equal to either 0 or 1) due to numerical diffusion. Because this is a purely advective case ($\mathrm{Pe} = \infty$), there should be no diffusive mixing and the concentration should be either 0 or 1 (black or white) throughout the entire domain. However, the striations of pure material quickly become thinner than the grid size, especially in the completely chaotic case ($T = 1.6$). As a consequence, cells receive particles from both the initially white and the initially black domains, resulting in the gray regions in the figure, an example of unintended numerical diffusion.

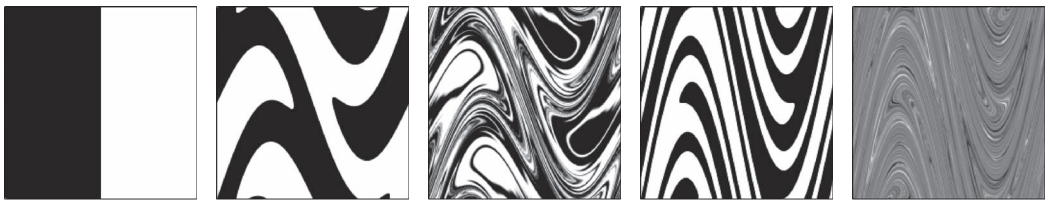

(a) Initial Condition (b) $T = 0.8$, Period=1 (c) $T = 0.8$, Period=5 (d) $T = 1.6$, Period=1 (e) $T = 1.6$, Period=5

FIG. 3. Spatial concentration profiles under TPSF without diffusion (Pe $= \infty$) calculated using the MM method with $\Delta t = T$ and $N_x = 180$.

D. Numerical results

To assess the accuracy of the MM method, we use the reference (or "exact") solution from an appropriate method that is known to be accurate. For Pe $= \infty$, we use a particle tracking (PT) method instead of the GS method as the reference solution. This is because the initial concentration profile (Figure 3(a)) is discontinuous and so, in the absence of diffusion, remains discontinuous for $t > 0$. Thus, the spectral expansion (9) suffers from the Gibbs phenomenon. However, for any Pe $< \infty$, the concentration profile will be continuous for $t > 0$ and the GS method (with enough modes) will be sufficiently accurate. For the PT method, 100 points are uniformly distributed in each cell (as in Figure 1(a)) and tracked backwards in time[4,34] to determine their initial cell and, hence, the corresponding concentration value (i.e., 0 or 1). The concentration in each cell is the average of the concentration at those 100 points. We found that 100 points provide a nearly exact result for the grid used here.

To begin, we compare the MM method in the absence of diffusion (Pe $= \infty$) for $T = 0.8$ and for three values of the time step. First, we consider a time step Δt equal to the period T. That is, particles are mapped a full period forward, which is the approach used by Singh *et al.*[32] and Christov *et al.*[28] For the other two cases, we consider time steps of $\Delta t = T/4$ and $\Delta t = T/8$, which correspond to mapping the solution incrementally through each period. The error is calculated as the L^2 difference of the spatial concentration states with respect to the PT solution. Specifically, let $\boldsymbol{c}_{MM}$ and $\boldsymbol{c}_R$ be the vectors that gives the concentration at each grid point from the MM method and the reference PT method, respectively. Then, the error associated with the mapping method is defined as

$$\text{Error}(\boldsymbol{c}_{MM}|\boldsymbol{c}_R) = \frac{1}{\max(\boldsymbol{c}_R) - \min(\boldsymbol{c}_R)} \sqrt{\frac{1}{N_x N_y} \sum_{j=1}^{N_x N_y} \left[\boldsymbol{c}_R^{(j)} - \boldsymbol{c}_{MM}^{(j)}\right]^2}. \tag{12}$$

Figure 4(a) shows that the error, which in this case is a result of numerical diffusion from the mapping method, increases with the number of periods. This is because numerical diffusion is compounded with each multiplication of $\boldsymbol{\Phi}_{t_0 \to t_0 + \Delta t}$. Using $\Delta t = T$ results in less numerical diffusion than $\Delta t < T$ because only one multiplication by a mapping matrix is required to advance the concentration by one period. The error saturates after several periods because the mixture becomes mostly homogenized in the chaotic region (see Figure 3(c)). Note that computing the solution at $t = T$ using the MM method with $\Delta t = T$ is, in fact, equivalent to computing it with the PT method with forward particle tracking. This explains why the error in Figure 4(a) for $\Delta t = T$ is very low initially (over the first period) since, with sufficiently large n, backward and forward particle tracking are equivalent. Additionally, Figure 4(b) shows that numerical diffusion (as inferred through the error in the solution) decreases as N_x increases, as expected.

Since the PT method cannot be used for Pe $< \infty$, we now use the GS method (with a large number of modes) as the reference solution. To ensure that the number of modes $(2N + 1)^2$ is sufficient, we calculate the difference between the final states (after five periods) of the GS solution with N and $2N$. We require that the difference be orders of magnitude smaller than the difference between the GS method (with N) and the MM method to ensure that the GS solution is sufficiently close to the exact solution. For TPSF, the appropriate value of N depends only on Pe. For our

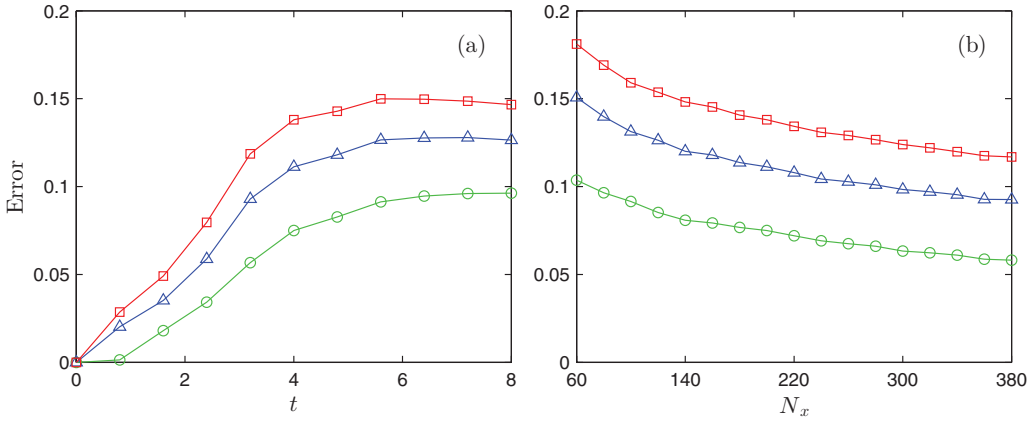

FIG. 4. Plots of the error for the MM method with $\Delta t = T$ (circle), $\Delta t = T/4$ (triangle), and $\Delta t = T/8$ (square) as (a) a function of time for $N_x = 200$ and (b) a function of N_x after five periods, compared to the reference PT solution. TPSF with $T = 0.8$ and $\mathrm{Pe} = \infty$.

simulations, we set $N = 75$ for $\mathrm{Pe} = 10^3$ and $N = 150$ for $\mathrm{Pe} \geq 10^4$. For these values of N, the maximum concentration difference between final states with N and $2N$ modes is on the order of 10^{-11} after five periods. Given that the concentration range is $0 \leq c \leq 1$, these values of N are more than adequate. At higher Péclet numbers, the final states have finer structure (striations), which requires more modes to accurately resolve.

Next, to demonstrate the effect of physical diffusion on mixing, Figure 5 shows the final states of TPSF with $T = 0.8$ after five periods for various values of Pe. These figures were obtained using the MM method with $\Delta t = T/8$ ($\Delta t = T$ for $\mathrm{Pe} = \infty$). Diffusion washes out the thin concentration striations and even parts of the regular (KAM) regions that exist at $\mathrm{Pe} = \infty$. Qualitatively, these concentration profiles look nearly identical to the results for both the GS method and the MM method with $\Delta t = T$, which are not shown. However, there are subtle differences, as shown in Figures 6 and 7.

In Figure 6, the concentration along a typical vertical slice is shown for the GS method and the MM method with $\Delta t = T$ and $\Delta t = T/8$. The qualitative behavior is very similar regardless of the computational approach, but the MM method with $\Delta t = T/8$ is more accurate than the MM method with $\Delta t = T$ when compared to the GS method. In particular the MM method with $\Delta t = T$ does not resolve the local extrema as well as the MM method with $\Delta t = T/8$. There are several other anomalies for $\Delta t = T$ as well, such as the deviation from the smooth curve around $y = 0.47$ in Figure 6(a) and the variation at $y = 0.18$ and $y = 0.67$ in Figure 6(d).

In Figure 7, the differences between the concentration after five periods computed by the MM method (with $\Delta t = T/8$) and the GS method are shown, and the maximum and average relative errors

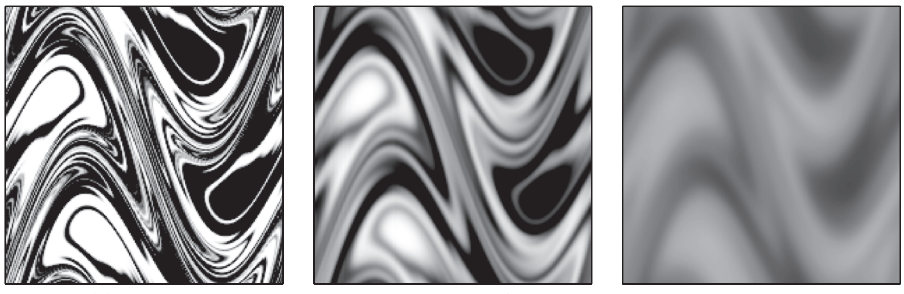

(a) $\mathrm{Pe} = \infty$ (b) $\mathrm{Pe} = 10^4$ (c) $\mathrm{Pe} = 10^3$

FIG. 5. Final states after five periods of TPSF with $T = 0.8$ and (a) pure advection and (b, c) advection-diffusion. Calculated using the MM method with $N_x = 180$ and $\Delta t = T/8$ ($\Delta t = T$ for $\mathrm{Pe} = \infty$ in (a)).

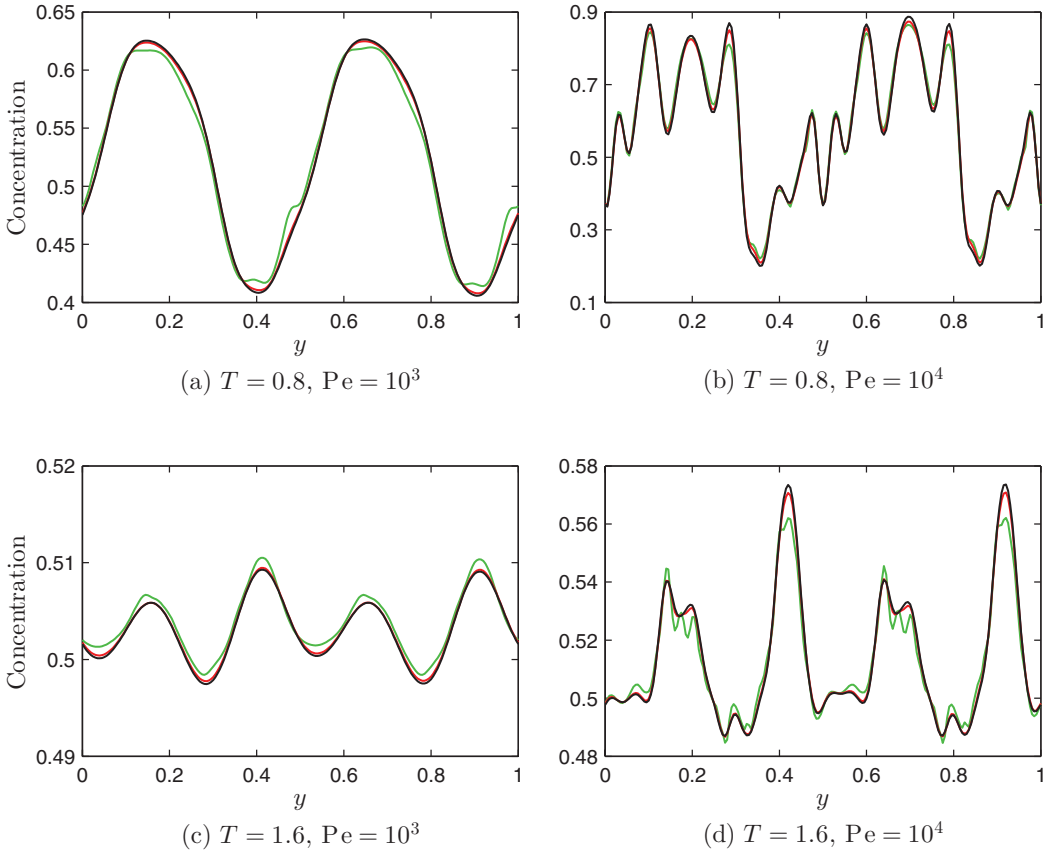

FIG. 6. (a)–(d) Typical vertical slice (at $x = 0.25$) of the concentration profile, shown after five periods and computed with the MM method with $\Delta t = T$ (lighter gray, green), the MM method with $\Delta t = T/8$ (darker gray, red), and the GS method (black). For all three methods, $N_x = 160$. Note vertical scale changes between plots.

are presented in Table II. In Figure 7, the white areas of the domain correspond to the maximum relative error (as given in Table II), and the black areas of the domain correspond to an error of 0. Both the maximum and average relative error are normalized by the difference between the maximum and minimum concentration in the domain after five periods. It appears that, as is the case in Figure 6, most of the error occurs near extrema in concentration, which is most easily seen when comparing Figure 7(b) to Figure 3(c). While not shown in Figure 7, the error in the solution by the MM method with $\Delta t = T$ looks very similar to the case with $\Delta t = T/8$ (for the same T and Pe), except that the $\Delta t = T$ case has slightly blurrier features and a larger maximum error (as indicated in Table II). The maximum error in Table II may seem somewhat large for $\Delta t = T/8$ (around 3.6% in one case),

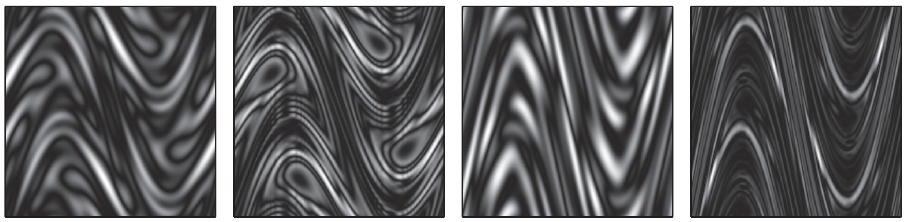

FIG. 7. (a)–(d) Relative error (with respect to the GS solution) in the final concentration profile after five periods for the MM method with $\Delta t = T/8$ and $N_x = 200$. White corresponds to the maximum relative error (as given in Table II), while black corresponds to an error of 0.

TABLE II. Maximum and average relative errors in the final concentration state after five periods for the MM method with $N_x = 200$, where the relative error is determined by normalizing the error by the difference between the maximum and minimum concentration across the entire domain.

		$T = 0.8$ Pe $= 10^3$	$T = 0.8$ Pe $= 10^4$	$T = 1.6$ Pe $= 10^3$	$T = 1.6$ Pe $= 10^4$
$\Delta t = T$	Maximum relative error	0.102	0.103	0.106	0.138
	Average relative error	0.0287	0.0265	0.0397	0.0279
$\Delta t = T/8$	Maximum relative error	0.0185	0.0357	0.0207	0.0281
	Average relative error	0.00468	0.00975	0.00666	0.00519

but the error is very small when averaged across the entire domain. This is consistent with Figure 6 in which the curves match very well almost everywhere. For higher spatial resolution and smaller Δt, the maximum error approaches 0, suggesting the convergence of this numerical method. For instance, the maximum error for $T = 0.8$ and Pe $= 10^4$ with $\Delta t = T/40$ and $N_x = 700$ decreases to 1.3% with an average error of 0.37%.

Next, we consider how to minimize the error in the solution computed with the MM method, using the GS solution as the reference solution in Eq. (12). Figure 8 shows how the error depends on the spatial resolution, as quantified by N_x. For $\Delta t = T$, there is little change in the error as N_x increases. This is because, even for $N_x = 50$, the operator splitting error associated with taking $\Delta t = T$ is much greater than the error due to the given spatial resolution. For $\Delta t < T$, increasing N_x reduces the error. For N_x small, $\Delta t = T/8$ has a larger error than $\Delta t = T/4$, since $\Delta t = T/8$ requires more matrix multiplications per period and thus compounds the numerical diffusion. However, as N_x is increased, the error for $\Delta t = T/8$ eventually becomes smaller than the error for $\Delta t = T/4$ as the numerical diffusion inherent in each mapping matrix multiplication is negligible compared

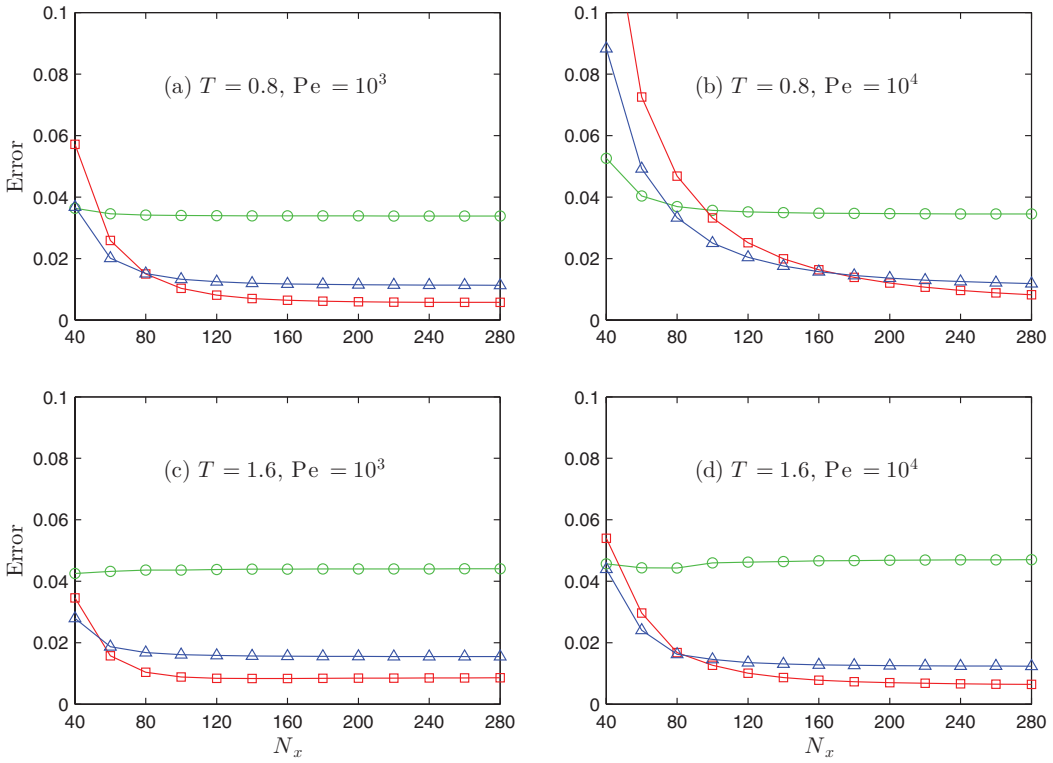

FIG. 8. (a)–(d) Dependence of the error on the number of grid cells N_x at $t = 4.8$ (i.e., 6 periods for $T = 0.8$ and 3 periods for $T = 1.6$) for the MM method with $\Delta t = T$ (○), $\Delta t = T/4$ (△), and $\Delta t = T/8$ (□).

to the error due to operator splitting. For $\mathrm{Pe} = 10^3$ (Figures 8(a) and 8(c)), the error no longer decreases above a certain spatial resolution because, as for $\Delta t = T$, the error at this point is almost entirely due to operator splitting, so increasing the number of grid cells has little effect overall. For $T = 0.8$ and $\mathrm{Pe} = 10^4$ (Figure 8(b)), a spatial resolution above which the error no longer decreases is never reached for $\Delta t < T$, though we expect that at a sufficiently large N_x this will occur as well. $\mathrm{Pe} = 10^4$ requires higher spatial resolution to minimize numerical diffusion because the structure of the concentration profile at such a large Pe is dominated by chaotic advection, which produces fine striations and lamellar structures in the flow that require more grid cells to resolve.

III. MIXING

One application of our efficient and, as we have shown above, accurate numerical approach to advection-diffusion in chaotic flows is addressing the interplay between chaos and molecular diffusion, a topic of considerable ongoing interest.[39,42,50] To quantify the amount of mixing in the domain, we recall that $\boldsymbol{c}(t)$ denotes the vector of concentration values in each of the $N_x N_y$ grid cells, and we use the discrete *intensity of segregation*[51] (level of "unmixedness") as our metric,

$$I_d(\boldsymbol{c}) = \frac{1}{N_x N_y \bar{c}(1-\bar{c})} \sum_{j=1}^{N_x N_y} \left[\boldsymbol{c}^{(j)}(t) - \bar{c}\right]^2, \tag{13}$$

where $\bar{c}$ is the spatial average of the concentration. Note that I_d is a function of time since $\boldsymbol{c}$ is a function of time. For our simulations, $\bar{c} = 0.5$ (recall Figure 3(a)), although it has been shown that different initial conditions will result in the same long-time mixing rate of the system.[52–55] Because of this, $I_d = 1$ at $t = 0$. For a completely mixed system, $I_d = 0$.

A. Degree of global mixing

Consider I_d as a function of time for several different Péclet numbers and computed using both the MM method (with $\Delta t = T$ and $\Delta t = T/8$) and the GS method. As shown in Figure 9, I_d decays exponentially with time, with the smallest Pe resulting in the sharpest slope (best mixing), as expected. More importantly, the MM method (with both values of Δt) and the GS method give nearly identical results, with the GS method yielding a slightly smaller degree of mixing. This is because numerical diffusion in the MM method induces additional mixing that is not physically present in the flow. However, this can be minimized with a sufficiently fine grid so that essentially all diffusional mixing is from physical diffusion and not numerical diffusion. Since the curves for all

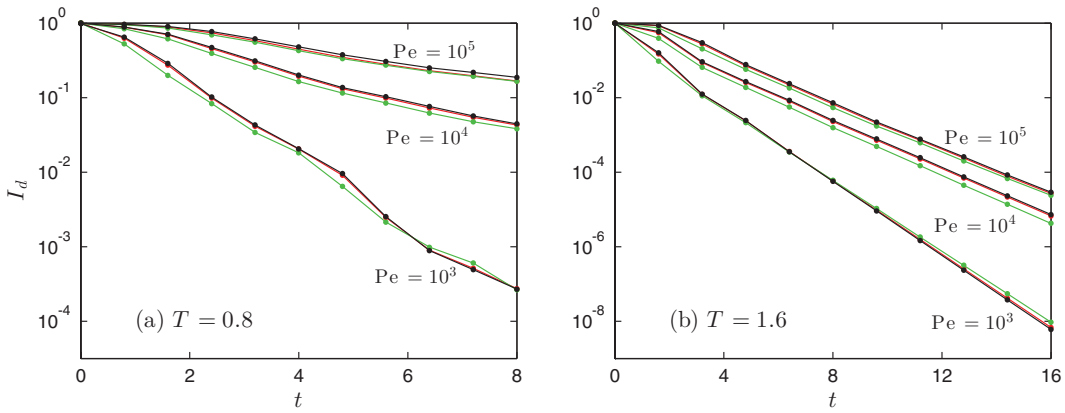

FIG. 9. Degree of advective-diffusive mixing (as measured by I_d in Eq. (13)) as a function of time in TPSF with (a) $T = 0.8$ and (b) $T = 1.6$ for $\mathrm{Pe} = 10^3$, 10^4, and 10^5 as computed by the MM method with $\Delta t = T$ (lighter gray, green), the MM method with $\Delta t = T/8$ (darker gray, red), and the GS method (black). $N_x = 400$ for both the MM and GS methods.

three methods match closely, it is clear that the choice of splitting time step Δt in the MM method is not critical for this gross measure of mixing, i.e., the splitting error does not significantly affect the value of I_d.

B. Comparison to the numerical-as-molecular diffusion mapping method (ND method)

It is instructive to compare the operator splitting approach of incorporating diffusion (the MM method from Sec. II) to the recently proposed approach of interpreting numerical diffusion as molecular diffusion in the mapping method (ND method of Gorodetskyi *et al.*[16]). The latter approach suggests that the advection-diffusion problem (1) for a given Péclet number can be solved using the purely advective mapping method (Eq. (4)) with a properly chosen spatial resolution. To obtain the correct "amount" of diffusion, it has been shown both numerically[16,41] and analytically[56] that, in two dimensions, the number of grid cells N_xN_y should grow linearly with Pe.

In Figure 10, we compare the MM solution to the ND solution by considering I_d for TPSF with $T = 1$ and $\mathrm{Pe} = 1.4 \times 10^5$. The ND method requires $N_x = N_y = 100$ for $\mathrm{Pe} = 1.4 \times 10^5$,[16] while we use $N_x = N_y = 400$ for the MM method to minimize the effect of numerical diffusion. There is good agreement in the evolution of mixing as computed by these two methods, indicating that both can accurately describe the overall mixing characteristics of the flow.

While the ND method accurately describes the quality of mixing in this flow, it is unable to resolve the details of the concentration profile. The final concentration profiles computed by the ND method and the MM method with $\Delta t = T/10$ for TPSF with $T = 1$ and $\mathrm{Pe} = 1.4 \times 10^5$ are shown in Figure 11. Again we note that the ND method[16] fixes the number of grid cells (at $N_x = N_y = 100$) when the Péclet number is specified to be 1.4×10^5, while higher spatial resolution can be used for the MM method at this same Péclet number. The concentration profile is not well resolved by the ND method, resulting in the coarse appearance of Figure 11(a). The low spatial resolution and loss of fine structure is more evident in a close-up of a portion of the domain (Figure 11(c)), especially when compared to the fine structures resolved using the MM method (Figure 11(d)), although the finite spatial resolution still results in non-smooth variation of the concentration at this level of magnification. Clearly, the MM method allows us to set the spatial resolution independently of the Péclet number in order to better resolve the fine structures.

C. Interplay between chaotic advection and diffusion

Now, we shift our focus to mixing in TPSF in the presence of diffusion and the interplay between mixing through chaotic advection and mixing across striations through diffusion. This interplay is crucial when considering certain physical situations, such as chemical reactions that can only occur when the reactants are in exact stoichiometric ratios.[19] For example, if a process

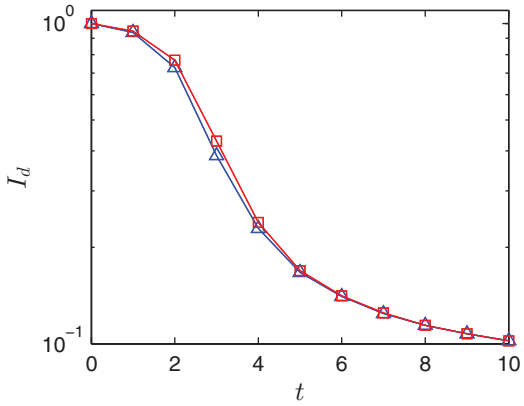

FIG. 10. Intensity of segregation as a function of time for TPSF with $T = 1$ and $\mathrm{Pe} = 1.4 \times 10^5$; computed using the MM method with $\Delta t = T/10$ and $N_x = N_y = 400$ (□) and the ND method with $N_x = N_y = 100$ (△).

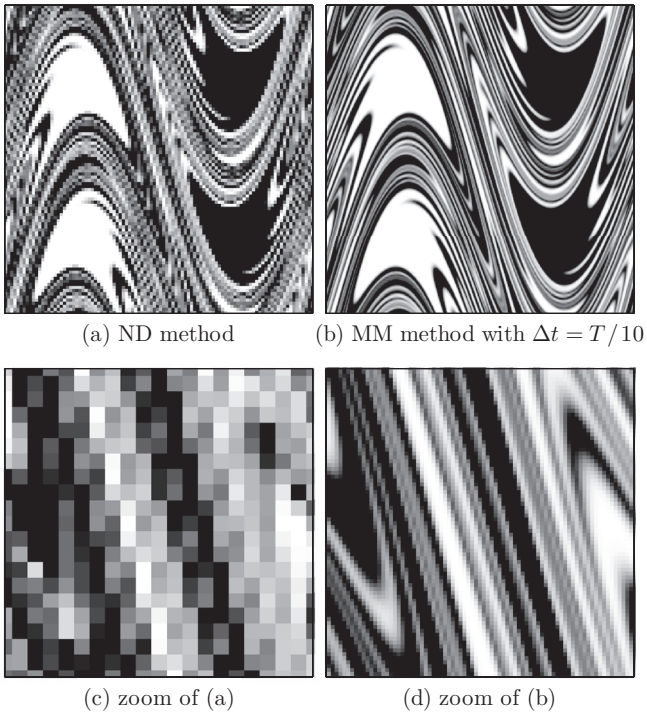

FIG. 11. Comparison of spatial concentration profiles computed by the ND and MM methods. In (a-b), spatial concentrations for TPSF with $T = 1$ and $\mathrm{Pe} = 1.4 \times 10^5$ after three periods. In (c-d), close-ups of (a-b) in the box $0.4 < x, y < 0.6$. For the ND method, $N_x = N_y = 100$ is set by the Péclet number; for the MM method, $N_x = N_y = 300$.

is diffusion dominated (low Pe), the reaction occurs quickly regardless of the underlying flow. However, if diffusivity is low, the chemical reaction only occurs at the interface between reactants, and the reaction rate will be primarily governed by the length of that interface, which depends on the degree of stretching and folding in the flow. Properly resolving a wide distribution of striation thicknesses is also important in atmospheric chemistry, which is often dominated by free radicals, where there is a spectrum of reactions with widely different rates and the interplay may involve a range of length scales.[57]

To begin, consider close-up views of the striations shown in Figure 12 for different conditions. For $\mathrm{Pe} = \infty$, the boundaries between white and black striations would be sharp if we were to solve Eq. (1) exactly. However, numerical diffusion from the MM method at the finite spatial resolution used for the simulations causes some fuzziness and jaggedness at the interfaces in Figure 12(a).

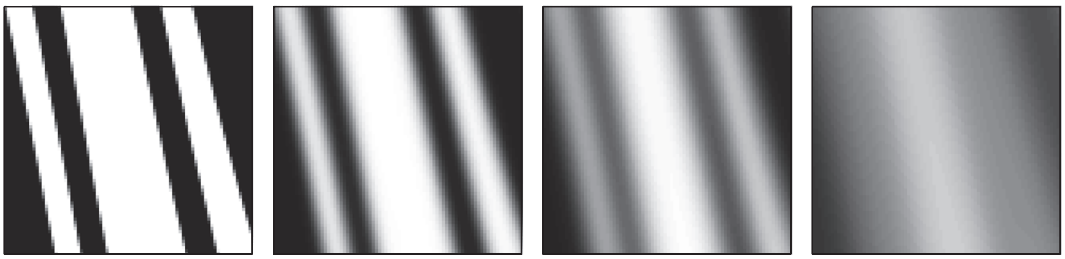

FIG. 12. (a)–(d) The role of diffusion is evident in close-up views ($0.424 < x < 0.62$ and $0.584 < y < 0.78$) of striations in TPSF with $T = 1.6$ after one period for various Pe calculated using the MM method with $N_x = 400$ and $\Delta t = T/8$ ($\Delta t = T$ for $\mathrm{Pe} = \infty$). For each Pe, the diffusional length scale ℓ^* for $t^* = T/2$ is indicated (see text).

Nevertheless, the striations are reasonably sharp, and the narrow black striations have a thickness of about $\ell_b = 0.019$. As we decrease Pe in Figures 12(a)–12(d), the blurring of the interface between the striations increases due to the increased efficacy of diffusion. For $\mathrm{Pe} = 2 \times 10^4$ (Figure 12(b)), the two narrow black striations are virtually unaffected by diffusion. Conversely, for $\mathrm{Pe} = 10^3$ (Figure 12(d)), the two narrow black striations are almost completely washed out after just one period.

A simple analysis of diffusion for a single striation of fixed width can be based on an analytic solution to the diffusion equation (i.e., Eq. (1) with $\boldsymbol{u} = 0$). Consider an initial condition like that in Figure 3(a), where the box has width 2ℓ (so each striation has width ℓ), and the white and black regions have concentrations of 1 and 0, respectively. Using periodic boundary conditions, the concentration profile is given by[58]

$$c(x,t) = \frac{1}{2} - \sum_{p=0}^{\infty} \frac{2}{(2p+1)\pi} \sin\left((2p+1)\pi \frac{x}{\ell}\right) \exp\left(-(2p+1)^2\pi^2 \frac{t}{\ell^2 \mathrm{Pe}}\right), \tag{14}$$

where x is the coordinate in the horizontal direction (with the concentration profile being identical in every horizontal cross-section), and the origin is located in the lower left corner of Figure 3(a). Equation (14) suggests that all modes decay as $\exp(-a^2 t/\ell^2 \mathrm{Pe})$, where $a = \pi$ for the dominant ($p = 0$) mode. We define ℓ^* to be the diffusional length scale, meaning that striations of thickness less than ℓ^* will "wash out" in a characteristic time t^*. A similar analysis for reaction-diffusion equations was presented by Muzzio and Ottino[54] where a reaction (between the two reactants) across a lamella (striation) would occur only if the lamella is of width less than ℓ^*. Based on the decay of the dominant mode in Eq. (14), a concentration striation of thickness ℓ^* will decay by a factor of $1/e^2$ in a time t^* that satisfies

$$\ell^* \approx \pi \sqrt{\frac{t^*}{2\mathrm{Pe}}}. \tag{15}$$

Using Eq. (15), the value for ℓ^* that causes the dominant mode to decrease by a factor of $1/e^2$ in half a period ($t^* = T/2$) can be estimated for each Pe as indicated in Figure 12.[59] As expected, a striation of thickness $\ell_b = 0.019$ at $\mathrm{Pe} = \infty$ is nearly washed out between $\mathrm{Pe} = 2 \times 10^4$ and $\mathrm{Pe} = 10^3$, for which this value of ℓ_b is between the corresponding values of ℓ^*. Although Eq. (14) cannot completely describe diffusion across striations since the striations are continuously narrowing due to stretching and folding, Eq. (15) indicates that striations on the order of ℓ^* are quickly homogenized by diffusion.

In comparison, Figure 13 shows the role of chaotic advection in the mixing process under TPSF with $T = 1.6$ and $\mathrm{Pe} = 10^5$, a case where the flow is chaotic and diffusion is weak. Again using Eq. (15) with $t^* = T/2$, we obtain $\ell^* = 0.0063$ at this Pe. In Figure 13(b), the narrowest striation has length $\approx$0.0056, which is very close to ℓ^*, indicating that diffusion begins to wash out the striations after $\approx$1.5 periods. Indeed, from 1.5 periods to 2 periods (Figures 13(b) and 13(c)), many individual striations go from being distinct to nearly washed out.

D. Evolution of the intensity of segregation

Based on our observations, we propose a heuristic model for the mixing metric as a function of time,

$$I_d(t) = \begin{cases} e^{-\beta t}, & 0 \le t \le \tau, \\ e^{-\beta\tau}\left[(1-B)e^{-\alpha(t-\tau)} + Be^{-\gamma(t-\tau)}\right], & t > \tau, \end{cases} \tag{16}$$

where B, τ, β, α, and γ are parameters that depend on T, Pe, or both. In general, we expect there to be little mixing from $t = 0$ to $t = \tau$, since initially the striations are too wide for diffusion to effectively mix across them. After a time τ has elapsed, the narrowing of the striations resulting from stretching and folding begins to play a role. Similar to reaction-diffusion systems,[54] for short times ($t < \tau$) mixing (or a chemical reaction) is localized at the initial interface between black and

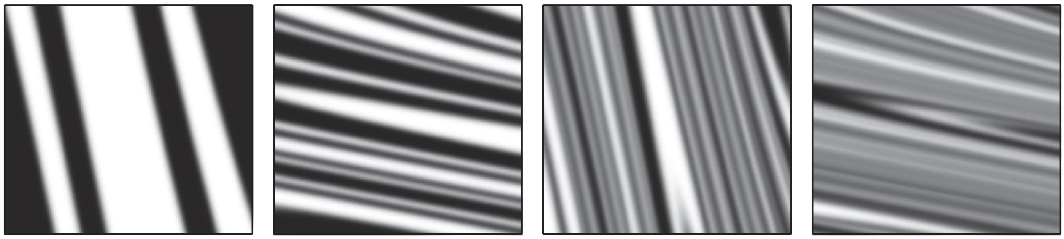

(a) 1 period (b) 1.5 periods (c) 2 periods (d) 2.5 periods

FIG. 13. (a)–(d) The effects of striation stretching by chaotic advection on mixing is evident in close-up views of striations for $T = 1.6$ and $\mathrm{Pe} = 10^5$; calculated using the MM method with $\Delta t = T/8$ and $N_x = 800$. During periods 1 and 2, the close-up box is $0.424 < x < 0.620$ and $0.584 < y < 0.780$; for periods 1.5 and 2.5, $0.804 < x < 1.000$ and $0.473 < y < 0.669$. For this case, the diffusional length scale $\ell^* = 0.0063$ (see text).

white material, while at long times ($t > \tau$) a distribution of striation thicknesses is generated by the flow, and global mixing becomes possible. For $t > \tau$, we divide the domain into chaotic and regular regions, as suggested by Toussaint and Carrière,[60] where the parameter B represents the ratio of the area of the regular regions to the total area of the domain, and $1 - B$ represents the ratio of the area of the chaotic region to the total area of the domain. The mixing metric has exponential decay in each region because diffusion always leads to exponential decay of the eigenmodes.[61] Initially, I_d evolves as $\exp(-\beta t)$ due to slow diffusional mixing localized at the initial interfaces between black and white material. After this initial transient of duration τ, I_d decays exponentially at a rate α in the chaotic regions, while it decays exponentially at a different rate γ in the regular regions (KAM islands), which is likely smaller than α because mixing in the regular regions is localized to the edges of the islands (see also Refs. 62 and 63).

Fits of Eq. (16) to $I_d(t)$ computed from the concentration profiles from the MM method simulations are shown in Figure 14. To obtain the parameter values used in Eq. (16), a nonlinear least-squares regression was implemented in MATLAB. First, for $T = 1.6$ and a given Pe, the parameters τ, β, and α were simultaneously fit according to Eq. (16) with $B = 0$, since there are no islands in this case. Then for $T = 0.8$ and $T = 1$, the parameters B, α, and γ were fit to Eq. (16) using the same β and τ from the $T = 1.6$ case, since β and τ are independent of T (see subsequent discussion). This procedure was repeated for each Pe. Thus, β and τ depend only on Pe, while B, α, and γ depend on both Pe and T (although it will be shown that B only depends weakly on Pe). It is evident from Figure 14 that Eq. (16) captures the evolution of the quality of mixing fairly well. Similar results were obtained for other values of T and Pe.

Looking more closely at the model parameters, τ represents the time at which the striations become narrow enough that diffusion washes them out. For example, considering the case of $T = 1.6$ and $\mathrm{Pe} = 10^5$ in Figure 13, after one period (Figure 13(a)) the striations are not yet narrow enough for diffusion to be effective at such a large Péclet number. However, in Figures 13(b) and 13(c), they are narrow enough for diffusion to effectively work across them. This means that the thickness of most striations is less than $\ell^* = 0.0063$, the diffusional length scale at $\mathrm{Pe} = 10^5$. Therefore, in this case, τ should be between 1 and 1.5 periods. In Figure 14(a), specifically the inset in the lower left corner, it is clear that, for these conditions, there is very little mixing for $t < 1.9$, which is indeed between 1 and 1.5 periods for $T = 1.6$. It is also evident from the inset in Figure 14(a) that τ and β are both independent of the period T. For β, this occurs because, in the beginning of the mixing process (from $t = 0$ to $t \approx 2$), the length of the interface between black and white (in the absence of diffusion) is similar for all T (not shown). Thus, since the striations are initially large, diffusional mixing is confined to the short interface between black and white material, and the initial mixing rate β is independent of T.

To further elucidate the crossover from mixing localized near the initial interfaces to mixing throughout the entire domain, the median of the striation thickness distribution ℓ_m (based on considering 100 horizontal cuts through the domain after each period in the absence of diffusion) is plotted in Figure 15(a) as a function of time for several different values of T. The median striation

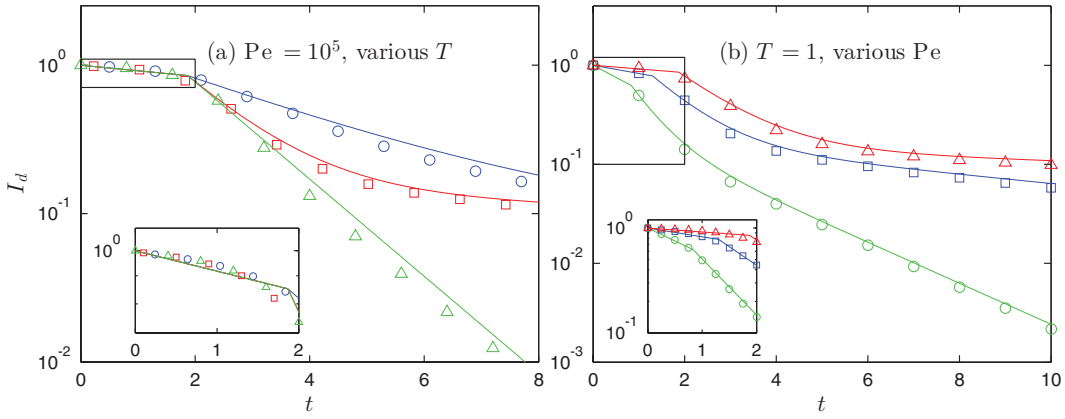

FIG. 14. (a) Intensity of segregation I_d vs. time in TPSF for $\mathrm{Pe} = 10^5$ and $T = 0.8$ (○), $T = 1$ (□), and $T = 1.6$ (△). (b) I_d vs. time for $T = 1$ and $\mathrm{Pe} = 10^3$ (○), $\mathrm{Pe} = 10^4$ (□), and $\mathrm{Pe} = 10^5$ (△). In both panels, all data points were calculated using the MM method with $\Delta t = T/40$ and $N_x = 600$. For each Pe and T, data are fit (solid curves) according to Eq. (16). Higher temporal resolution plots for $0 < t < 2$ are shown in the lower left corner inset in each plot.

thickness is nearly independent of T with $\ell_m \sim \exp(-1.6t)$, indicating that the striation thickness distribution is similar for all T (except for the presence of islands, which will not affect the median of the striation thickness distribution). Self-similarity of striation thickness distributions is seen in other systems as well.[55] This implies that τ is independent of T since the thickness of striations will become comparable to ℓ^* at the same time for all T. The values of τ (calculated for $T = 1.6$, but used for all T) are shown in Figure 15(b) as a function of Pe. Since significant mixing across the striations occurs after $t = \tau$ (when most striations have thickness less than ℓ^*), $\ell^* \sim \exp(-1.6\tau)$. Equation (15) indicates that $\ell^* \sim 1/\sqrt{\mathrm{Pe}}$, so $e^{\tau} \sim \mathrm{Pe}^{-3.2}$, which agrees reasonably well with the trend in Figure 15(b).

Higher Pe values result in slower mixing, as shown in Figure 14(b) for $T = 1$ and several values of Pe. For small Pe, diffusion quickly penetrates the regular regions, which leads to the steady decay of I_d, even at large times. For larger Pe, the decay of I_d appears to saturate as time goes on because even after the chaotic region is (nearly) homogenized, mixing remains hindered by the presence of islands. Furthermore, mixing in the chaotic region does not always occur at the same rate. From Figure 14(a), we see that the α's (slopes of I_d on the log-linear plot for t slightly larger than τ) for $T = 1$ and $T = 1.6$ are similar and both are larger than α for $T = 0.8$, yet TPSF with $T = 1$ has larger

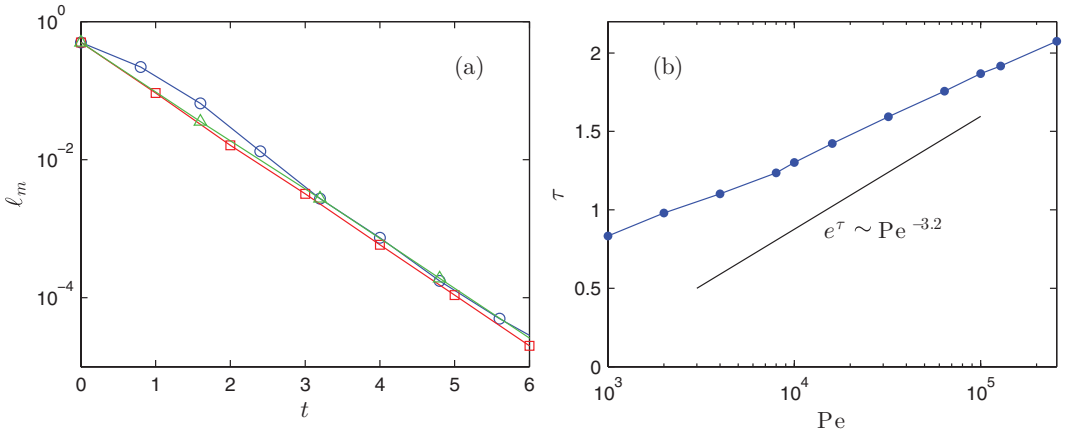

FIG. 15. (a) Median striation thickness ℓ_m for $\mathrm{Pe} = \infty$ is plotted vs. time for $T = 0.8$ (○), $T = 1$ (□), and $T = 1.6$ (△). (b) τ from Eq. (16) is plotted vs. Pe (●) where the solid line shows the predicted slope (see text).

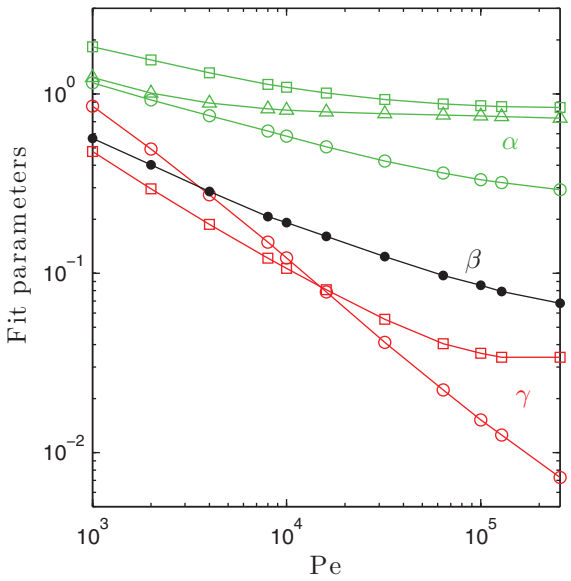

FIG. 16. The parameters α (lighter gray, green), γ (darker gray, red), and β (black) used to fit Eq. (16) to the simulation results plotted as functions of Pe for $T = 0.8$ (○), $T = 1$ (□), and $T = 1.6$ (△). $T = 1.6$ is not shown for γ because in this case $B = 0$ and γ drops out of Eq. (16). Since β is independent of T, it is only plotted once.

islands than TPSF with $T = 0.8$ (compare Figure 11 to Figure 5). Therefore B for $T = 1$ is larger than B for $T = 0.8$, and I_d for $T = 1$ decreases slower at later times than I_d for $T = 0.8$, as expected from Eq. (16).

As a result of β and τ being independent of the period T of TPSF, the impact of different T on the mixing metric can only be observed after the initial transient and depends on the interaction of chaotic advection, diffusion, and the presence of islands, which are reflected in the parameters α, γ, and B. Turning first to B, the ratio of the area of the regular regions to the total area, it is evident that B depends on T but only weakly depends on Pe (not shown). While there is slight variation in B with Pe (as diffusion erodes the boundaries of the islands), the values of B closely match the actual area of the islands, as calculated from the final states in the absence of diffusion (Pe $= \infty$).[64] Specifically, for $T = 1$, B (as estimated by fitting Eq. (16) to simulation results) decreases from 0.31 to 0.17 for Pe between 10^3 and 3×10^5, while the actual area of the islands is $B_{\text{exact}} \approx 0.22$ at Pe $= \infty$. For $T = 0.8$, B increases from 0.06 to 0.11 for the same range of Pe, while $B_{\text{exact}} \approx 0.08$.

As shown in Figure 16, β, α, and γ are all smooth monotonically decreasing functions of Pe. Because both β and γ are related to mixing along limited interfaces (inter-material boundaries at the initial time for β, and the interfaces at the periphery of regular regions for γ), they are the same order of magnitude. Meanwhile, α is a measure of diffusion enhanced by chaotic advection, which generates narrower and narrower striations having more and more interface length, so $\alpha > \gamma \sim \beta$ in general.

The evolution of the quality of mixing in TPSF, which is governed by the interplay between chaotic advection and diffusion, can be accurately described by Eq. (16). The size of regular regions and the striation thickness distribution in the domain are determined by the advective velocity field. On the other hand, diffusion, which ultimately leads to complete homogenization in this system, controls the rate β of mixing at the initial interfaces between black and white material, determines the diffusional length scale ℓ^*, and homogenizes striations that are less than $\mathcal{O}(\ell^*)$ thick at rate α. The median of the striation thickness distribution can be compared to ℓ^* to determine when (i.e., the time $t = \tau$ in our approach) diffusional mixing of the striations dominates the stretching and folding of striations by TPSF. Once diffusion homogenizes all striations in the chaotic region, mixing is dominated by the presence of regular regions, which can slow down the rate of homogenization.

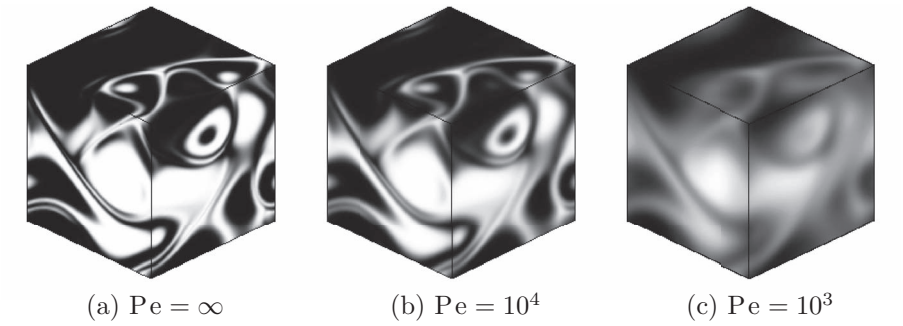

FIG. 17. (a)–(c) Concentration profiles for ABC flow computed using the MM method (with $N_x = N_y = N_z = 150$ and $\Delta t = 0.1$) at $t = 5$ for different Péclet numbers.

IV. APPLICATION TO 3D CHAOTIC MIXING

Advection-diffusion in 3D chaotic flows has been of interest recently,[65,66] as increasingly powerful computational resources have allowed for integration of these flows. The MM method we described in Sec. II A can be applied to the three-dimensional version of Eq. (1). To demonstrate this, consider a standard 3D chaotic flow, the Arnold–Beltrami–Childress (ABC) flow,

$$\boldsymbol{u}(x, y, z) = (A \sin z + C \cos y)\,\hat{\boldsymbol{x}} + (B \sin x + A \cos z)\,\hat{\boldsymbol{y}} + (C \sin y + B \cos x)\,\hat{\boldsymbol{z}} \qquad (17)$$

defined in the cube $0 \le x, y, z \le 2\pi$ with periodic boundary conditions. This velocity field, originally proposed in 1965 by Arnold,[67] is a Beltrami flow, i.e., $\boldsymbol{u} \times (\nabla \times \boldsymbol{u}) = \boldsymbol{0}$, and is an exact solution of the three-dimensional steady state Euler equations of inviscid fluid flow.[67,68] It was also studied independently by Childress[69] (with $A = B = C = 1$) as an example of the kinematic dynamo effect. Hénon[70] showed numerically that for $A = \sqrt{3}$, $B = \sqrt{2}$, and $C = 1$, this flow exhibits partially chaotic dynamics, so we use these values as well. In generalizing the MM method to 3D, the mapping matrix $\boldsymbol{\Phi}_{t_0 \to t_0 + \Delta t}$ becomes an $N_x N_y N_z \times N_x N_y N_z$ matrix, and we seed n^3 tracer particles uniformly in each grid cell (similar to Figure 1(a)).

In Figure 17, the concentration profiles are shown at $t = 5$ for $\mathrm{Pe} = \infty$, 10^4, and 10^3. Initially, half the domain ($x < 1/2$) is black (concentration 0) and the other half ($x > 1/2$) is white (concentration 1). For these simulations, $\Delta t = 0.1$ and $N_x = N_y = N_z = 150$. It is evident in Figure 17 that both chaotic and regular regions are present, with the unmixed regions taking the form of KAM tubes, which are 3D analogs of KAM islands.[71,72] For smaller values of Pe, diffusion causes mixing across the KAM tube boundaries and erodes what would otherwise be unmixed regions.

Looking more closely at mixing in ABC flow, Figure 18 shows the intensity of segregation I_d as a function of time for three values of Pe. In three dimensions, Eq. (13) becomes

$$I_d(\boldsymbol{c}) = \frac{1}{N_x N_y N_z \bar{c}(1 - \bar{c})} \sum_{j=1}^{N_x N_y N_z} \left[\boldsymbol{c}^{(j)}(t) - \bar{c}\right]^2, \qquad (18)$$

where, as before, $\bar{c}$ is the spatial average of the concentration and $\boldsymbol{c}(t)$ denotes the vector containing the concentration values in each of the $N_x N_y N_z$ grid cells. As in Figure 9, I_d decreases exponentially with the best mixing occurring for the smallest Pe. Like the results for two-dimensional TPSF shown in Figure 14(b), diffusion dominates for small Pe, penetrating the regular (KAM) regions, while for large Pe the decay of I_d is slowed by the presence of regular regions that hinder diffusion.

V. SUMMARY AND FUTURE WORK

Mapping methods have shown promise as simple and effective numerical approaches for studying chaotic advection. In the present work, we have shown that diffusion can be easily incorporated into these methods, extending their reach to advection-diffusion problems. Specifically, we benchmarked the MM method of Christov *et al.*[28] and incorporated subperiod splitting time steps. This

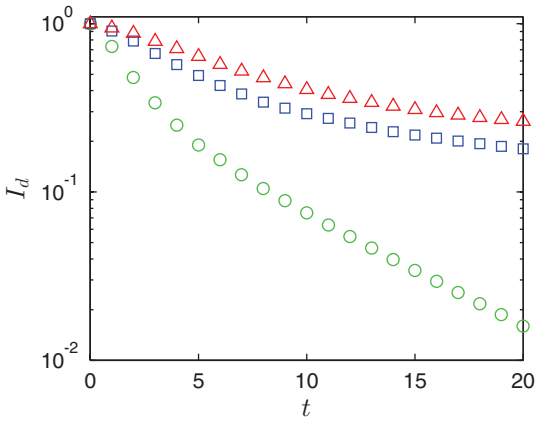

FIG. 18. Degree of advective-diffusive mixing (as measured by I_d in Eq. (18)) as a function of time in ABC flow for $\mathrm{Pe} = 10^3$ (o), $\mathrm{Pe} = 10^4$ (□), and $\mathrm{Pe} = 10^5$ (△) calculated using the MM method with $\Delta t = 0.1$ and $N_x = N_y = N_z = 150$.

numerical method is able to accurately capture both the concentration profiles and the quality of advective-diffusive mixing (measured via Danckwerts' intensity of segregation) in chaotic flows. The MM method, with a splitting time step smaller than the period of the flow, results in a quantitatively accurate solution, while a time step equal to the period (convenient for many problems and also less computationally expensive) provides qualitatively accurate results. Thus, the modified mapping method allows us to incorporate diffusion into the mapping framework in a relatively simple way that is still physically accurate, which, in general, can be difficult using other methods.

Using the MM method, we conducted a detailed study of the interplay between chaotic advection and diffusion in mixing under TPSF, a canonical two-dimensional chaotic flow. By considering the evolution of striations in the concentration profile, we showed that it is possible to determine qualitatively when the evolution of the concentration profile is dominated by stirring due to chaotic advection versus mixing by diffusion. It is also possible to study when diffusion and chaotic advection complement each other to produce faster mixing. An analytic expression for the quality of mixing in the domain as a function of time was proposed. This expression quantitatively captures the interplay between chaotic advection and diffusion, describing the rate and quality of mixing as the concentration profile evolves over both short and long time scales.

We also showed that the modified mapping method extends directly to three dimensions, using an ABC flow as an example. It is a straightforward exercise to benchmark and validate the method in 3D as we have done above for 2D. Furthermore, it is of interest to determine whether our analysis of the interplay between chaotic advection and diffusion, as modeled by Eq. (16), generalizes to three dimensions and if it also fits experimental results. Finally, extending these ideas beyond advection-diffusion of passive scalars to *active* scalars is another avenue for future work.

ACKNOWLEDGMENTS

This research was funded by NSF (Grant No. CMMI-1000469). I.C.C. was additionally supported, in part, by NSF (Grant No. DMS-1104047).

[1] G. Metcalfe, M. F. M. Speetjens, D. R. Lester, and H. J. H. Clercx, "Beyond passive: Chaotic transport in stirred fluids," in *Advances in Applied Mechanics*, edited by E. van der Giessen and H. Aref (Elsevier, Amsterdam, 2012), Vol. 45, pp. 109–188.
[2] R. S. Spencer and R. M. Wiley, "The mixing of very viscous liquids," J. Colloid Sci. **6**, 133–145 (1951).
[3] C. S. Hsu, *Cell-to-Cell Mapping: A Method of Global Analysis for Nonlinear Systems*, Applied Mathematical Science Vol. 64 (Springer-Verlag, New York, 1987).
[4] L. Wang, Y. Fan, and Y. Chen, "Animation of chaotic mixing by a backward Poincaré cell-map method," Int. J. Bifurcation Chaos **11**, 1953–1960 (2001).
[5] G. Froyland and K. Padberg, "Almost-invariant sets and invariant manifolds – connecting probabilistic and geometric descriptions of coherent structures in flows," Physica D **238**, 1507–1523 (2009).

[6] G. Froyland, N. Santitissadeekorn, and A. Monahan, "Transport in time-dependent dynamical systems: Finite-time coherent sets," Chaos **20**, 043116 (2010).
[7] G. Froyland, K. Padberg, M. H. England, and A. M. Treguier, "Detection of coherent oceanic structures via transfer operators," Phys. Rev. Lett. **98**, 224503 (2007).
[8] S. Ross and P. Tallapragada, "Detecting and exploiting chaotic transport in mechanical systems," in *Applications of Chaos and Nonlinear Dynamics in Science and Engineering - Vol. 2*, Understanding Complex Systems, edited by Santo Banerjee, Lamberto Rondoni, and Mala Mitra (Springer, Berlin/Heidelberg, 2012), pp. 155–183.
[9] P. D. Anderson and H. E. H. Meijer, "Chaotic mixing analyses by distribution matrices," Appl. Rheol. **10**, 119–133 (2000).
[10] P. G. M. Kruijt, O. S. Galaktionov, P. D. Anderson, G. W. M. Peters, and H. E. H. Meijer, "Analyzing mixing in periodic flows by distribution matrices: Mapping method," AIChE J. **47**, 1005–1015 (2001).
[11] O. S. Galaktionov, P. D. Anderson, G. W. M. Peters, and C. L. Tucker, "A global, multi-scale simulation of laminar fluid mixing: The extended mapping method," Int. J. Multiphase Flow **28**, 497–523 (2002).
[12] I. Klapper, "Shadowing and the role of small diffusivity in the chaotic advection of scalars," Phys. Fluids A **4**, 861–864 (1992).
[13] C. A. Fletcher, *Computational Techniques for Fluid Dynamics* (Springer-Verlag, New York, 1988), Vol. 1.
[14] A. Quarteroni, R. Sacco, and F. Saleri, *Numerical Mathematics*, Texts in Applied Mathematics Vol. 37 (Springer, Berlin/Heidelberg, 2000).
[15] M. K. Singh, M. F. M. Speetjens, and P. D. Anderson, "Eigenmode analysis of scalar transport in distributive mixing," Phys. Fluids **21**, 093601 (2009).
[16] O. Gorodetskyi, M. Giona, and P. D. Anderson, "Exploiting numerical diffusion to study transport and chaotic mixing for extremely large Péclet values," EPL **97**, 14002 (2012).
[17] For example, when solving the advection equation with a finite-difference scheme, there is an "effective equation" that the scheme solves exactly.[13,14] This effective equation usually contains a diffusion term with a diffusivity that depends on both the spatial resolution and the velocity in a nontrivial way. For a spatially-dependent velocity field, the effective equation is *not* equivalent to the advection-diffusion equation (1) with constant diffusivity. Moreover, most numerical schemes also contain *artificial (numerical) dispersion* or higher-order (non-Laplacian) dissipation in the effective equation.
[18] J. M. Ottino, *The Kinematics of Mixing: Stretching, Chaos, and Transport*, Cambridge Texts in Applied Mathematics Vol. 3 (Cambridge University Press, Cambridge, 1989).
[19] J. M. Ottino, "Lamellar mixing models for structured chemical reactions and their relationship to statistical models; Macro- and micromixing and the problem of averages," Chem. Eng. Sci. **35**, 1377–1381 (1980).
[20] R. W. Bilger, "Turbulent flows with nonpremixed reactants," in *Turbulent Reacting Flows*, Topics in Applied Physics Vol. 44, edited by Paul Libby and Forman Williams (Springer, Berlin/Heidelberg, 1980), pp. 65–113.
[21] G. M. Faeth and G. S. Samuelsen, "Fast reaction nonpremixed combustion," Prog. Energy Combust. Sci. **12**, 305–372 (1986).
[22] J. G. Franjione and J. M. Ottino, "Symmetry concepts for the geometric analysis of mixing flows," Philos. Trans. R. Soc. London, Ser. A **338**, 301–323 (1992).
[23] M. Liu, F. J. Muzzio, and R. L. Peskin, "Quantification of mixing in aperiodic flows," Chaos, Solitons Fractals **4**, 869–893 (1994).
[24] L. D. Landau and E. M. Lifshitz, *Fluid Mechanics* (Butterworth-Heinemann, Oxford, 1959).
[25] J.-L. Thiffeault, "Scalar decay in chaotic mixing," Lect. Notes Phys. **744**, 3–35 (2008).
[26] F. J. Muzzio and M. Liu, "Chemical reactions in chaotic flows," Chem. Eng. J. **64**, 117–127 (1996).
[27] A. D. Stroock, S. K. W. Dertinger, A. Ajdari, I. Mezic, H. A. Stone, and G. M. Whitesides, "Chaotic mixer for microchannels," Science **295**, 647–651 (2002).
[28] I. C. Christov, J. M. Ottino, and R. M. Lueptow, "From streamline jumping to strange eigenmodes: Bridging the lagrangian and Eulerian pictures of the kinematics of mixing in granular flows," Phys. Fluids **23**, 103302 (2011).
[29] S. Cerbelli, V. Vitacolonna, A. Adrover, and M. Giona, "Eigenvalue-eigenfunction analysis of infinitely fast reactions and micromixing regimes in regular and chaotic bounded flows," Chem. Eng. Sci. **59**, 2125–2144 (2004).
[30] S. Cerbelli, A. Adrover, F. Creta, and A. Giona, "Foundations of laminar chaotic mixing and spectral theory of linear operators," Chem. Eng. Sci. **61**, 2754–2761 (2006).
[31] J. G. Franjione and J. M. Ottino, "Feasibility of numerical tracking of material lines and surfaces in chaotic flows," Phys. Fluids **30**, 3641–3643 (1987).
[32] M. K. Singh, O. S. Galaktionov, H. E. H. Meijer, and P. D. Anderson, "A simplified approach to compute distribution matrices for the mapping method," Comput. Chem. Eng. **33**, 1354–1362 (2009).
[33] M. K. Singh, T. G. Kang, H. E. H. Meijer, and P. D. Anderson, "The mapping method as a toolbox to analyze, design, and optimize micromixers," Microfluid. Nanofluid. **5**, 313–325 (2008).
[34] Z. B. Stone and H. A. Stone, "Imaging and quantifying mixing in a model droplet micromixer," Phys. Fluids **17**, 063103 (2005).
[35] Indeed, Christov *et al.*,[28] use backward particle tracking, so the denominator of $\mathbf{\Phi}^{(i,j)}_{t_0\to t_0+\Delta t}$ is the total number of tracers from any cell that end in cell i instead of the total number of tracers that start in any cell, as in Eq. (2) and Ref. 32. Again, since the flow is incompressible and each grid cell is the same size, a large enough n makes this difference negligible.
[36] W. F. Ames, *Numerical Methods for Partial Differential Equations*, 2nd ed. (Academic Press, New York, 1977).
[37] E. Ott, Y. Du, K. R. Sreenivasan, A. Juneja, and A. K. Suri, "Sign-singular measures: Fast magnetic dynamos, and high-Reynolds-number fluid turbulence," Phys. Rev. Lett. **69**, 2654–2657 (1992).
[38] Y. Du and E. Ott, "Fractal dimensions of fast dynamo magnetic fields," Physica D **67**, 387–417 (1993).
[39] R. T. Pierrehumbert, "Tracer microstructure in the large-eddy dominated regime," Chaos, Solitons Fractals **4**, 1091–1110 (1994).
[40] A. Chertock, C. R. Doering, E. Kashdan, and A. Kurganov, "A fast explicit operator splitting method for passive scalar advection," J. Sci. Comput. **45**, 200–214 (2010).

[41] O. Gorodetskyi, M. Giona, and P. D. Anderson, "Spectral analysis of mixing in chaotic flows via the mapping matrix formalism: Inclusion of molecular diffusion and quantitative eigenvalue estimate in the purely convective limit," Phys. Fluids **24**, 073603 (2012).
[42] S. W. Jones, "Interaction of chaotic advection and diffusion," Chaos, Solitons Fractals **4**, 929–940 (1994).
[43] R. Glowinski, "Finite element methods for incompressible viscous flow," in *Numerical Methods for Fluids (Part 3)*, Handbook of Numerical Analysis Vol. 9, edited by P. G. Ciarlet and J. L. Lions (Elsevier, Amsterdam, 2003).
[44] While it is possible to derive a version of Eq. (8) that uses a second-order operator splitting procedure (e.g., the "symmetric" strange splitting), the gains in accuracy are negligible because the time stepping used for both the advection and diffusion substeps is first-order accurate. Moreover, there is no theoretical error analysis establishing the time-accuracy of the mapping method used in the advection step.
[45] S. L. Brunton and C. W. Rowley, "Fast computation of finite-time Lyapunov exponent fields for unsteady flows," Chaos **20**, 017503 (2010).
[46] D. R. Lester, M. Rudman, G. Metcalfe, and H. M. Blackburn, "Global parametric solutions of scalar transport," J. Comput. Phys. **227**, 3032–3057 (2008).
[47] R. Courant and D. Hilbert, *Methods of Mathematical Physics* (John Wiley & Sons, New York, 1953), Vol. I.
[48] L. N. Trefethen, *Spectral Methods in* MATLAB (Society for Industrial and Applied Mathematics, Philadelphia, PA, 2000).
[49] E. L. Paul, V. A. Atiemo-Obeng, and S. M. Kresta, *Handbook of Industrial Mixing: Science and Practice* (Wiley-Interscience, Hoboken, NJ, 2004), Chap. 3.
[50] A. Adrover, S. Cerbelli, and M. Giona, "On the interplay between advection and diffusion in closed laminar chaotic flows," J. Phys. Chem. A **105**, 4908–4916 (2001).
[51] P. V. Danckwerts, "The definition and measurement of some characteristics of mixtures," Appl. Sci. Res., Sect. A **3**, 279–296 (1952).
[52] F. J. Muzzio and J. M. Ottino, "Evolution of a lamellar system with diffusion and reaction: A scaling approach," Phys. Rev. Lett. **63**, 47–50 (1989).
[53] F. J. Muzzio and J. M. Ottino, "Dynamics of a lamellar system with diffusion and reaction: Scaling analysis and global kinetics," Phys. Rev. A **40**, 7182–7192 (1989).
[54] F. J. Muzzio and J. M. Ottino, "Diffusion and reaction in a lamellar system: Self-similarity with finite rates of reaction," Phys. Rev. A **42**, 5873–5884 (1990).
[55] F. J. Muzzio, P. D. Swanson, and J. M. Ottino, "The statistics of stretching and stirring in chaotic flows," Phys. Fluids A **3**, 822–834 (1991).
[56] G. Metcalfe, "Effective Pe in mapping," personal communication (2012).
[57] J. H. Seinfeld and S. N. Pandis, *Atmospheric Chemistry and Physics: From Air Pollution to Climate Change* (Wiley-Interscience, New York, 1997).
[58] R. Haberman, *Elementary Applied Partial Differential Equations: With Fourier Series and Boundary Value Problems* (Prentice Hall, Upper Saddle River, NJ, 1998).
[59] We use $t^* = T/2$ because times longer than this would result in significant stretching and folding, thus drastically changing the thickness of the initial striation.
[60] V. Toussaint and P. Carrière, "Diffusive cut-off scale of fractal surfaces in chaotic mixing," Int. J. Bifurcation Chaos **9**, 443–454 (1999).
[61] W. Liu and G. Haller, "Strange eigenmodes and decay of variance in the mixing of diffusive tracers," Physica D **188**, 1–39 (2004).
[62] S. Cerbelli, A. Adrover, and M. Giona, "Enhanced diffusion regimes in bounded chaotic flows," Phys. Lett. A **312**, 355–362 (2003).
[63] J. P. Gleeson, "Transient micromixing: Examples of laminar and chaotic stirring," Phys. Fluids **17**, 100614 (2005).
[64] The area of the islands, B_{exact}, is determined by considering the striation thickness distribution for $\text{Pe} = \infty$ (calculated by considering 100 horizontal cuts through the domain) and determining the percentage by area of striations that are "significantly thicker" than the other striations.
[65] X. Z. Tang and A. H. Boozer, "A Lagrangian analysis of advection-diffusion equation for a three dimensional chaotic flow," Phys. Fluids **11**, 1418–1434 (1999).
[66] K. Ngan and J. Vanneste, "Scalar decay in a three-dimensional chaotic flow," Phys. Rev. E **83**, 056306 (2011).
[67] V. I. Arnold, "Sur la topologie des écoulements stationnaires des fluides parfaits," C. R. Acad. Sci. Paris **261**, 17–20 (1965).
[68] T. Dombre, U. Frisch, J. M. Greene, M. Hénon, A. Mehr, and A. M. Soward, "Chaotic streamlines in the ABC flows," J. Fluid Mech. **167**, 353–391 (1986).
[69] S. Childress, "New solutions of the kinematic dynamo problem," J. Math. Phys. **11**, 3063–3076 (1970).
[70] M. Hénon, "Sur la topologie des lignes de courant dans un cas particulier," C. R. Acad. Sci. Paris A **262**, 312–314 (1966).
[71] M. Feingold, L. P. Kadanoff, and O. Piro, "Passive scalars, three-dimensional volume-preserving maps, and chaos," J. Stat. Phys. **50**, 529–565 (1988).
[72] H. A. Kusch and J. M. Ottino, "Experiments on mixing in continuous chaotic flows," J. Fluid Mech. **236**, 319–348 (1992).